

Fuel Variation Effects in Propagation and Stabilization of Turbulent Counter-Flow Premixed Flames

Ehsan Abbasi-Atibeh¹

Department of Mechanical Engineering,
McGill University,
Montreal, QC H3A 0C3, Canada
e-mail: ehsan.abbasi@mail.mcgill.ca

Sandeep Jella

Siemens Canada Limited,
Montreal, QC H9P 1A5, Canada;
Department of Mechanical Engineering,
McGill University,
Montreal, QC H3A 0C3, Canada
e-mail: sandeep.jella@siemens.com

Jeffrey M. Bergthorson

Department of Mechanical Engineering,
McGill University,
Montreal, QC H3A 0C3, Canada
e-mail: jeff.bergthorson@mcgill.ca

Sensitivity to stretch and differential diffusion of chemical species are known to influence premixed flame propagation, even in the turbulent environment where mass diffusion can be greatly enhanced. In this context, it is convenient to characterize flames by their Lewis number (Le), a ratio of thermal-to-mass diffusion. The work reported in this paper describes a study of flame stabilization characteristics when Le is varied. The test data are comprised of $Le \ll 1$ (hydrogen), $Le \approx 1$ (methane), and $Le > 1$ (propane) flames stabilized at various turbulence levels. The experiments were carried out in a hot exhaust opposed-flow turbulent flame rig (HOTFR), which consists of two axially opposed, symmetric jets. The stagnation plane between the two jets allows the aerodynamic stabilization of a flame and clearly identifies fuel influences on turbulent flames. Furthermore, high-speed particle image velocimetry (PIV), using oil droplet seeding, allowed simultaneous recordings of velocity (mean and rms) and flame surface position. These experiments, along with data processing tools developed through this study, illustrated that in the mixtures with $Le \ll 1$, turbulent flame speed increases considerably compared to the laminar flame speed due to differential diffusion effects, where higher burning rates compensate for the steepening average velocity gradient and keeps these flames almost stationary as bulk flow velocity increases. These experiments are suitable for validating the ability of turbulent combustion models to predict lifted, aerodynamically stabilized flames. In the final part of this paper, we model the three fuels at two turbulence intensities using the flamelet generated manifolds (FGM) model in a Reynolds-averaged Navier–Stokes (RANS) context. Computations reveal that the qualitative flame stabilization trends reproduce the effects of turbulence intensity; however, more accurate predictions are required to capture the influences of fuel variations and differential diffusion. [DOI: 10.1115/1.4041136]

1 Introduction

Most of the world's required energy in industrial systems and transportation is provided through combustion. The lean premixed combustion is a promising approach for reducing pollutants, such as nitric oxides (NO_x) and soot. Lean premixed ultra-low-emission gas-turbine engines (GTE) play a significant role in the power generation industry. However, fuel-flexibility of these lean premixed combustors is also an important feature of these engines, as lean premixed turbulent combustion of mixtures with different chemistry and transport properties, originating from various nonrenewable (fossil fuels) and renewable sources, brings large uncertainty in the design process and operability properties of these engines. Fuel-flexibility addresses two main issues: (1) difference in chemical properties of the combustible mixture (fuel + air), which is clearly seen in hydrogen-enrichment of hydrocarbon fuels in laminar flame studies [1,2] and (2) difference in transport properties (diffusivity of deficient species), which plays an important role in the propagation of premixed flames. The effect of transport properties is clearly seen in the study carried out by Boschek et al. [3], where it was illustrated that, with increasing the hydrogen (H_2) concentration in methane (CH_4) flames, the laminar flame speed increased linearly while the turbulent flame speed rapidly diverged from the behavior of laminar flames at higher H_2 concentrations, and increased nonlinearly toward much higher velocities.

A turbulent flame is stretched due to the bulk hydrodynamic strain (K_s) and the stretch effects of turbulent eddies in the flow, which can be expressed by flame curvature (κ) [4]: $K = S_L \kappa + K_s$, where K is the flame stretch rate. The effects of stretch are highly important in the propagation of premixed flames in both laminar flames [5–7] and in turbulent flames [8–11].

The stretch sensitivity in flame propagation is shown by the Lewis number (Le), which defines the balance between the thermal diffusivity of the mixture (α) and the mass diffusivity of the deficient reactant (D) (fuel in lean, and oxidant in rich combustion) at the flame front. The disparity between thermo-diffusive properties, α and D , is also known as “differential diffusion.”

Many researchers have studied the effects of Le in the propagation of turbulent flames [12–16]. A number of studies reported differential diffusion effects with a focus on measuring the burning velocity and consumption speed of turbulent flames [9,17], as well as local flamelet measurements [18,19]. However, the time-averaged measurements of turbulent flame properties reported in the majority of these studies do not necessarily yield local information on the physics of turbulent flame propagation at an instantaneous scale [20]. Therefore, in this study, statistical methods are used to describe instantaneous local properties of turbulent premixed flames, such as flame position and turbulent flame speed, based on probability density functions (PDF). These experiments investigate the effects of differential diffusion on the propagation of turbulent premixed flames of lean H_2 -air, CH_4 -air, and C_3H_8 -air mixtures, representative of low ($Le \ll 1$), unity ($Le \approx 1$), and high ($Le > 1$) Lewis numbers, respectively.

These experiments are conducted in the powerfully simple geometry of hot exhaust opposed-flow turbulent flame rig (HOTFR) [21–23]. The rig has a compact geometry, excellent

¹Corresponding author.

Manuscript received July 11, 2018; final manuscript received July 16, 2018; published online October 29, 2018. Editor: Jerzy T. Sawicki.

optical accessibility, and well-defined boundary conditions, where aerodynamically stabilized lifted flames are not affected by conductive heat loss to the burner. Furthermore, the counter-flowing hot exhaust gases enable turbulent flames to be stabilized at higher bulk flow velocities and turbulence intensities, which enables turbulent flame experiments to be extended to higher Karlovitz numbers (Ka) and assures sustaining turbulent combustion in the thin reaction zone of the Borghi diagram [24]. These characteristics make the rig convenient both for diagnostics and computational studies and allows experiments closer to relevant conditions of GTEs and other combustors.

The experiments provide data to evaluate design tools in the field of turbulent combustion, specifically fuel-flexibility. Accordingly, computations for all three fuels at two different turbulence intensities (lowest and highest for each fuel) were carried out to complement the experiments and obtain additional insight. The computations make use of the flamelet-progress variable approach, a regularly used framework in the industry due to its low computational overhead. The economy comes from being able to tabulate chemistry based on the assumption that a turbulent flame may be considered as an ensemble of locally laminar “flamelets,” whose structure can be precalculated for a range of strain rates, equivalence ratios, and heat loss effects [25,26], parametrized by a reaction progress variable, and referenced during run time. *A priori* flamelet calculations use “flamelet generated manifolds” (FGM) [27] as a chemistry reduction technique while creating a database of strained flamelets in composition space. Since finite-rate chemistry effects can be incorporated at the flame front, this method is capable of predicting lifted flames. It is of interest, therefore, to evaluate its ability to reproduce the flame stabilization trends observed in the experiments described in this paper.

2 Experimental Method

2.1 Turbulent Counter-Flow Burner. In these experiments, lean premixed turbulent flames of H_2 -air at equivalence ratio (ϕ) = 0.19, CH_4 -air at ϕ = 0.6, and C_3H_8 -air at ϕ = 0.7 are stabilized in a HOTFR under atmospheric pressure. These mixtures are representative of distinct Lewis numbers of $Le \ll 1$, $Le \approx 1$, and $Le > 1$, respectively. The rig consists of two axially opposed,

symmetric turbulent round jets. The two jets issue from a stainless steel nozzle on one side (the reactant mixture side) and a ceramic burner nozzle on the opposing side (hot product side). The schematic of HOTFR is illustrated in Fig. 1. The premixed fuel and air mixture from the bottom nozzle accelerates toward the test section and the flame impinges against hot exhaust gases from the ceramic burner at the top. Balance of momentum at the stagnation plane between the two jets allows the formation of an aerodynamically stabilized flame. The excellent optical access allows well-defined boundary conditions and clearly identifies fuel influences on turbulent flames. The stabilizing effect of the hot products allows higher turbulence conditions.

The premixed fuel and air nozzle assembly at the bottom consists of two concentric sets of plenum and nozzles. The inner nozzle, with an exit diameter of $d_N = 20$ mm and the contraction ratio of 9, is attached to a plenum of diameter 60 mm, and delivers the premixed fuel and air mixture to feed the turbulent flame. The nozzle centerline bulk flow velocity at the nozzle exit (U_{NE}) varies with the values of $0.9 \text{ m/s} \leq (U_{NE}) \leq 5.6 \text{ m/s}$ in these experiments. The outer nozzle (co-flow nozzle) provides a flow of nitrogen (N_2), as a co-flow to shroud the flame from the surrounding environment and stabilize the edge of the flame. Furthermore, the flame is only studied within the radial boundaries of $-0.25 \leq (r/d_N) \leq 0.25$, away from the flame edge and the shear layer with the co-flow. A portion of air delivered to the bottom nozzle is passed through an atomizer, where Laskin nozzles are used to generate atomized oil droplets as seeding particles in laser diagnostics. In order to generate high intensity turbulent flow at the test domain, a multicircular turbulence generating plate (TGP) is used [21,28]. The plate has five jets with the hole diameter of 1.7 mm on the radius of 15 mm, with a percent open area of 0.35%. The TGP is located in the inner plenum at a vertical distance from the nozzle exit of 123 mm. The exhaust gases are generated using a water-cooled preburner inside a ceramic nozzle with a contraction ratio of 6.25, and at a vertical distance from the nozzle exit of 90 mm. CH_4 -air mixtures at equivalence ratios of $0.75 \leq \phi \leq 0.85$ are used to feed the ceramic burner. The nozzle exit velocity (U_{CB}) and the equivalence ratio of the mixture is adjusted to balance the momentum, and deliver the exhaust gases at nozzle exit temperatures (T_{CB}) of $1400 \text{ K} < T_{CB} < 1900 \text{ K}$.

The required fuel, air, and inert flows are delivered to the rig using mass flow controllers, calibrated using a Bios DryCal ML-

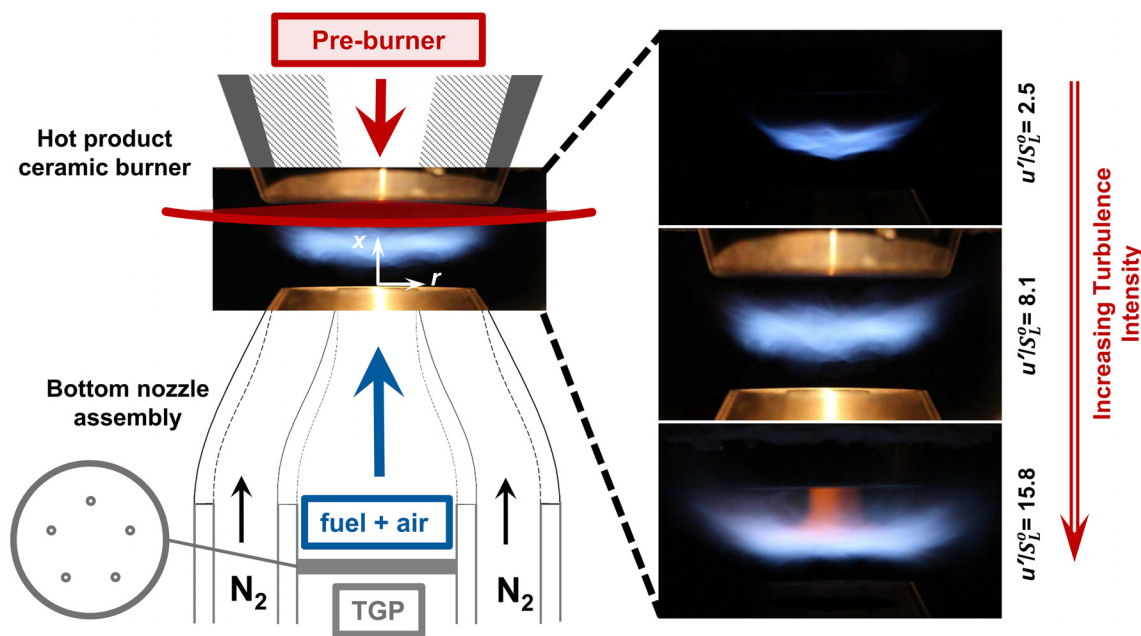


Fig. 1 Schematic of HOTFR, and stabilized CH_4 -air turbulent flames at increasing turbulence intensities

Table 1 Properties of the laminar flames

	C ₃ H ₈ + air	CH ₄ + air	H ₂ + air
ϕ	0.7	0.6	0.19
Le	1.860	0.976	0.334
δ_L (mm)	0.247	0.433	0.516
T_{ad} (K)	1889	1668	898
S_L^0 (cm/s)	19.7	11.5	8.75
S_L (at 576 K) (cm/s)	37.8	22.1	16.8

800-44 dry-piston calibrator to reduce uncertainty in mixture composition. Multiple opposed-flow jets of fuel and air, along with mixing vessels upstream of the nozzles help to maximize the mixing of fuel and air in a confined system. Furthermore, alumina (Al₂O₃) beads of 1 mm diameter are used upstream of the nozzles' exit in the plena to enhance the mixing.

Properties of fuel and air mixtures, used in this study, are listed in Table 1. Lewis number is calculated as: $Le = \alpha/D = \lambda/(\rho c_p D)$, where λ is thermal conductivity, c_p is the specific heat, and ρ is the density of the unburned reactants. Lewis number, adiabatic flame temperature (T_{ad}), and diffusive flame thickness ($\delta_L = \alpha/S_L^0$) are calculated using free-flame simulations in Cantera [29]. Unstretched laminar flame speed (S_L^0) is calculated by extrapolating the experimental results of the stretched laminar flame speeds reported in Ref. [30] to zero stretch.

The temperature of hot exhaust gases at the ceramic nozzle exit (T_{CB}) is measured using R-type thermocouples with three different wire (bead) diameters at 5 mm distance from the nozzle exit. The temperature readings are corrected for heat losses by extrapolating the measured temperature to a zero diameter. These calculations are done according to the details found in Refs. [31] and [32]. The estimated values of T_{CB} are reported in Table 2.

2.2 Particle Image Velocimetry and Processing Techniques.

In these experiments, the flow velocity field is quantified using two-dimensional high-speed particle image velocimetry (2D-PIV) within the imaged plane. In this method, a Nd:YLF laser at 527 nm-wavelength is used to illuminate oil droplets seeded into the flow, and the Mie scattered light is captured by a high-speed camera (see Fig. 2(b)). The imaging frequency ranges from 3.5 kfps to 14 kfps, and around 10,000 PIV image pairs are postprocessed using DaVis (a PIV software package) to calculate the velocity vector fields, as illustrated in Fig. 2(a). The smallest interrogation window used in PIV calculations is a 16×16 pixel grid, and the pixel-to-mm ratio is 30.7, yielding the PIV spatial resolution of $\approx 520 \mu\text{m}$.

Turbulent flow statistics of the mean (\bar{U}) and root-mean-square (rms) of velocity fluctuations (u' in axial direction and v' in radial direction) are calculated using instantaneous velocity vector

Table 2 Experimental conditions of turbulent C₃H₈-air flames at $\phi=0.7$, CH₄-air flames at $\phi=0.6$, and H₂-air flames at $\phi=0.19$

	U/S_L^0	u'/S_L^0	L/δ_L	Re_T	Ka_T	T_{CB} (K)
C ₃ H ₈	4.6	1.4	8.6	12.7	0.6	1504
	13.5	4.6	8.6	41.0	3.6	1824
	21.1	6.5	8.7	59.3	6.1	1916
	26.4	9.1	10.3	97.2	9.1	1907
CH ₄	8.8	2.5	5.7	14.4	1.7	1455
	25.1	8.1	5.5	45.3	9.9	1738
	35.8	11.2	5.2	59.9	16.8	1797
	48.7	15.8	6.6	106.6	25.1	1841
H ₂	13.1	3.5	4.1	12.4	2.6	1396
	32.2	10.9	4.5	42.8	13.8	1760
	42.9	16.2	5.2	73.5	22.9	1806
	63.4	19.8	4.8	81.7	32.7	1786

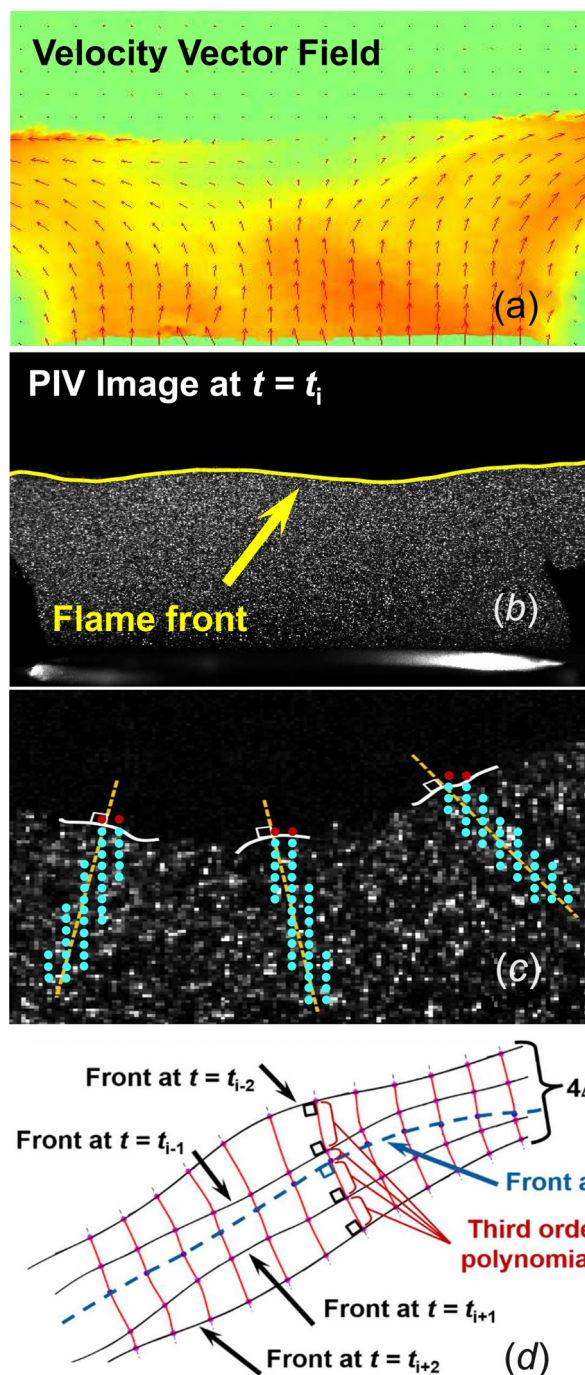


Fig. 2 Processing techniques using PIV images: (a) a sample velocity vector field (down-sampled for clarity), (b) a sample flame-front contour, (c) S_u measurement upstream of the flame front, and (d) 5 successive flame fronts centered at time t_i and a schematic showing S_F calculation

measurements through Reynolds decomposition: $U(r, x, t) = \bar{U}(r, x) + u(r, x, t)$, where r and x are radial and axial positions, respectively, at time t . The integral length scale (L) is also estimated using rms velocities by integrating the autocorrelation function up to the first zero-crossing as discussed in Refs. [33] and [34]: $L = \int_0^\infty R_{ii}(r, t) dr$. These results are listed in Table 2. In these experiments, turbulence intensity (u'/U) varies in the range of $44\% \leq (u'/U) \leq 60\%$. For uncertainty analysis of the flow velocity measurement, see Appendix.

Atomized canola oil droplets are used as seeding particles in PIV. At the flame front, oil droplets evaporate and disappear from

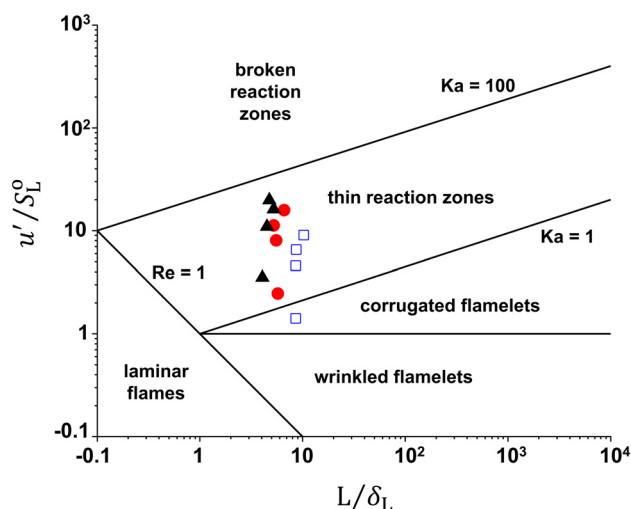


Fig. 3 Borghi diagram showing turbulent premixed combustion regimes: experimental region of C_3H_8 -air (\square), CH_4 -air (\bullet), and H_2 -air (\blacktriangle) flames

the Mie scattering images, which allow surface tracking methods to determine instantaneous flame-front contours within the plane of the laser sheet, as seen in Fig. 2(b). A similar method was used in previous studies for characterizing the flame front, see for example Refs. [35] and [36]. In flame front tracking, binarized PIV images are smoothed using edge preserving filtering, in order to reduce its sensitivity to noise. Laplacian of Gaussian filter is, then, applied to highlight regions of rapid intensity change, which is often used for edge detection. Zero crossings of the Laplacian of Gaussian filter correspond to positions of maximum gradient and localize the edges. Finally, instantaneous flame-front position is determined by tracking the flame front using an edge-finding algorithm. A similar method was used by Balusamy et al. [35] to track the propagation of spherical flames using an adopted filtering technique. Flame-front topology properties, such as normal directions to the flame front, flame surface density, and curvature are extracted from this data. For uncertainty analysis in flame surface tracking, see Appendix.

The two-component unburned gas velocity upstream of the flame front (S_u) is calculated based on the velocity vector field data in the vicinity of the normal lines to the flame front, as illustrated in Fig. 2(c). Flame position (Z_f) data are also used to calculate instantaneous apparent flame-front velocity within the imaged plane (S_F). As illustrated schematically in Fig. 2(d), in order to calculate S_F for a flamelet at time t_i , five successive flame contours (centered at t_i) are considered, and third-order polynomials are fit between each pair of successive fronts starting at the flamelet grid at time t_i and extending toward upstream and downstream flame fronts. These polynomials are calculated such that, they are perpendicular to both successive flame fronts, have the minimum length, and pass through the flamelet grid at time t_i , as well as the intersection grids of the flamelet's path and the flame-front contours specified by the minimum path length. Therefore, each flamelet's path consists of four continuous third-order polynomials, which are perpendicular to all five flame fronts and the total length is a minimum. The length of the estimated streamline is used to calculate the displacement velocity of the flamelet using a fourth-order finite difference method.

Although previously proposed methods [35,37] and the current approach utilize different image source and flame surface tracking methods, they all track the flamelet's path between consecutive flame-front contours to reconstruct the flame-front motion using successive image sequences. However, in the current approach, use of higher-order finite difference method in flame-front velocity calculations improves the signal-to-noise ratio.

S_F and S_u are, then, used to calculate instantaneous apparent local turbulent flame displacement velocity within the imaged plane and along the normal line to the flame surface contour (S_T) [20,38]: $S_T = (S_F + S_u) \cdot \mathbf{n}$. A similar method was also used and validated in Ref. [35] to measure local laminar burning velocity of stretched spherical flames.

Turbulent Karlovitz number (Ka_T) is a key nondimensional quantity describing turbulence-chemistry interactions. Ka_T is defined as the ratio of chemical time scale (τ_c) and the time scale related with the smallest eddies in the flow, known as Kolmogorov eddies, and is calculated as: $Ka_T = (L/\delta_L)^{-2} Re_T^{1.5}$, where Re_T is the turbulent Reynolds number.

Ka_T , rms velocities, L , and chemistry-related properties (δ_L and S_L^0) are suitable parameters in describing different regimes of turbulent premixed combustion in the Borghi diagram [24,39]. The experimental conditions listed in Table 2 are summarized in the Borghi diagram (Fig. 3). $Ka_T < 1$ indicates that the eddies of Kolmogorov length scale are significantly large compared to the flame thickness; hence, the eddies do not penetrate into the preheat zone and have only a wrinkling effect on the flame-front structure. This zone corresponds to the wrinkled and corrugated flamelet regions. On the other hand, $Ka_T > 1$ demonstrates that eddies of the Kolmogorov length scale have become sufficiently small, and they might penetrate into the reactive-diffusive flame structure. This region corresponds to the thin and broken reaction zones on the Borghi diagram. As illustrated in Fig. 3, the experimental conditions in this study are in the thin reaction zone of the Borghi diagram, to quantify measurements closer to the relevant operating conditions of GTEs.

2.3 Computational Model Description and Setup. The Favre-averaged equations for continuity, momentum, and energy were solved, together with the flamelet-progress variable equations using a commercial code, ANSYS 18.2. A Reynolds stress transport model is used for turbulence predictions, as it minimizes turbulence modeling issues with the mixed (laminar-turbulent) nature of the counter-flow system. Figure 4(a) shows contours of the fluctuating velocity field. Turbulent and laminar regions of the flow are reproduced and no spurious fluctuations can be seen in the laminar region. For brevity, the combustion model will be briefly summarized. The recent, comprehensive review of van Oijen et al. [27] may be consulted for full details, and the work by Jella et al. [40] for more specifics on the flamelet-generation method used in this article.

The flame is tracked by the mean reaction progress variable (\tilde{c}) and its variance (c'^2), which are used to convolve a conventional beta-pdf with the laminar (FGM) reaction rate. The progress

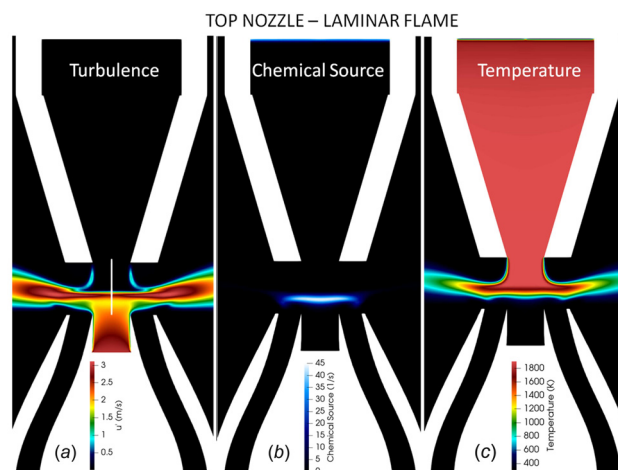


Fig. 4 Computational fluid dynamics model: (a) turbulent jet, (b) lifted flame front visualized by chemical source term, and (c) temperature contours

variable is defined as $\tilde{c} = \tilde{Y}_{\text{CO}} + \tilde{Y}_{\text{CO}_2}$ for the hydrocarbon flames, and $\tilde{c} = \tilde{Y}_{\text{H}_2\text{O}}$ for the hydrogen flames. Details on the closure for the source and sink terms in the transport of \tilde{c} and c''^2 may be found in Ref. [40]. In the limit of perfect mixing, the chemical source term is modeled as: $\tilde{\omega}_c = \int_0^1 \tilde{\omega}_c(\zeta) P(\zeta) d\zeta$ where ζ is the sample space variable for \tilde{c} , $\tilde{\omega}_c$ is the FGM reaction rate, and $P(\zeta)$ is the probability shape obtained from the beta-pdf. The FGM equations in composition space are solved as described by Nguyen et al. [41], assuming unity Lewis numbers. An important consequence that results from this transformation is the need to prescribe the scalar dissipation rate (SDR), χ_c , defined as $\chi_c = D_c(\nabla c \cdot \nabla c)$, which accounts for molecular mixing in composition space. In this work, the peak value of χ_c is computed from a physical space simulation, and an error function distribution [41] is used to calculate its variation through the flame. Since FLUENT is hardcoded to generate $Le = 1$ flamelets in c -space with an analytical SDR, we quantify the impact of the coordinate transformation using physical space solutions. Strained counter-flow flames corresponding to boundary conditions without TGP were calculated in Cantera as a cross-check of the Fluent $Le \neq 1$ physical space and c -space solutions, but for the sake of space, we refer to Ref. [40] for these results and reproduce the most relevant points below. The UCSD-San Diego 2016 mechanism has been used for all computations in this study.

Figure 5 summarizes the effect of $Le = 1$ on two important quantities that directly impact the flame speed: χ_c and $\tilde{\omega}_c$ for a lean ($\phi = 0.55$) methane flame. The main consequence of $Le = 1$ for lean methane flames is the lowering of reactivity due to the neglect of differential diffusion. This is seen “as a shifted peak for the SDR” in the range $0.2 < c < 0.8$ between the plots in Fig. 5. The differences between the physical space SDR and the error-function approximation do not appear to heavily influence the results in this case, although differences in species profiles should be expected. In the case of laminar hydrogen flames, much larger differences are seen between profiles of temperature and species (OH) in Fig. 6(b) and in heat release (\dot{Q}) in Fig. 7. \dot{Q} is observed to distribute over a larger range of c and reach a maximum c in the case of $Le \neq 1$. This implies that flamelet reaction rates that assume $Le = 1$ will under-predict the reaction rate. Therefore, while $Le = 1$ assumption might be a reasonable representation of the flame structure for methane flames, hydrogen flames are not likely to yield correct results with the present computational fluid dynamics methodology.

Accordingly, nonunity Le flamelets should be used, as noted by Donini et al. [26]. Goldin et al. [42] point out that in this case, the enthalpy equation is required to account for flamelet enthalpy changes and that a large turbulent eddy viscosity can easily mask molecular diffusivity influences. In order to investigate this further, major changes to the flamelet-progress variable implementation in the FLUENT code are required, or flamelets should be generated externally. For the present, we restrict discussion to our

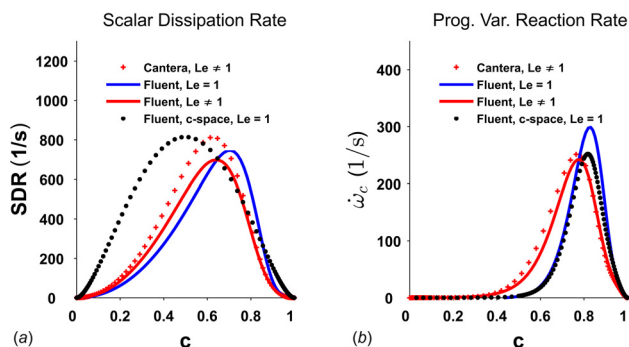


Fig. 5 Le influence on laminar and turbulent methane flames at $\phi = 0.55$: (a) SDR and (b) reaction rate

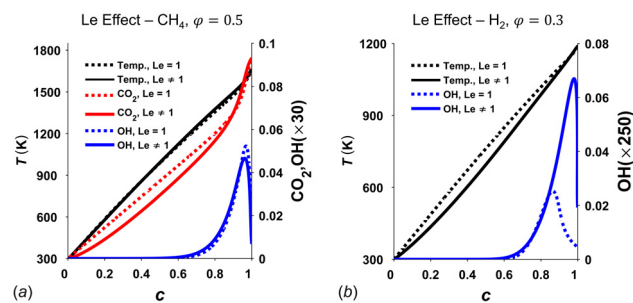


Fig. 6 Le influence on temperature and species: laminar flames of (a) methane and (b) hydrogen

findings with respect to the assumption of $Le = 1$ and reserve a more focused investigation of flamelet methods for the next step.

The flow and combustion model equations were discretized using second-order upwinding for convective terms and second-order central differencing for the diffusion terms. Two-dimensional axisymmetric forms of the equations were solved taking advantage of the statistically 2D axisymmetric flow. Boundary conditions for flow and turbulence were imposed using experimental measurements. Three-dimensional Reynolds-averaged Navier–Stokes (RANS) simulations with full resolution of TGP did not yield any significant advantage. In addition, the nozzle exit conditions were designed to be statistically isotropic to facilitate the most minimal computational domain. A simplified computational domain is shown for a propane flame in Fig. 4. The nature of the computations in this work are fundamental checks of the unity Le assumption (typically assumed in commercial codes such as FLUENT) in flamelet generation and its effect on predicting flame stabilization trends. A detailed analysis in 3D will be reserved for future work with more advanced turbulence modeling.

3 Results and Discussion

3.1 Results and Discussion: Experiments. The effects of stretch sensitivity and differential diffusion in propagation and stabilization of turbulent premixed flames through fuel variation are investigated in this study. In these experiments, instantaneous apparent flame position and velocity statistics within the imaged plane are extracted from PIV data. Over 10,000 PIV images are

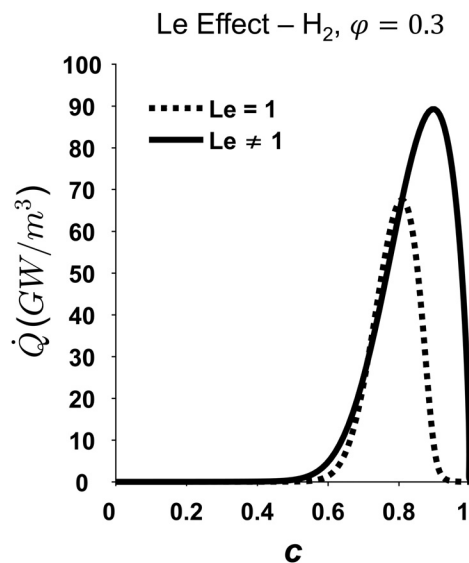


Fig. 7 Le influence on heat release: laminar hydrogen flames

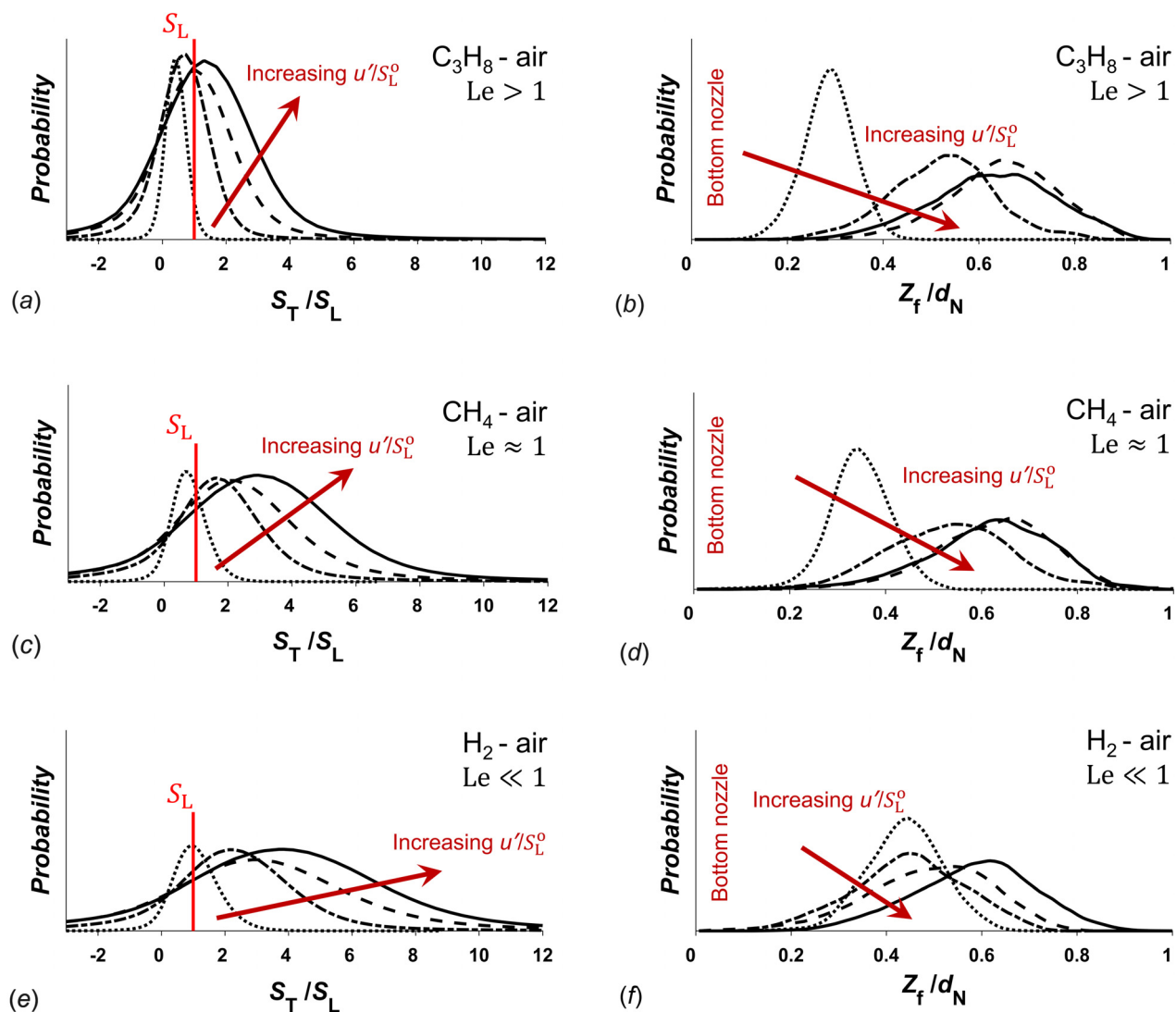


Fig. 8 Probability density functions of instantaneous leading edge displacement velocity (S_T) (left), and flame position (Z_f) (right) for: ((a) and (b)) C_3H_8 -air, ((c) and (d)) CH_4 -air, and ((e) and (f)) H_2 -air flames at increasing u'/S_L^0 . See Table 2 for u'/S_L^0 values.

processed for each experiment to improve the statistical accuracy, and, approximately, 10^6 data points are included to approach the probability density function of the statistics. For calculating the instantaneous apparent turbulent flame velocity within the plane of the laser sheet (S_T), vector summation of both unburned gas velocity upstream of the flame-front (S_u) and the instantaneous apparent flame-front velocity within the imaged plane (S_F) are considered in the direction perpendicular to the flame surface to quantify S_T . In these experiments, bulk flow velocity is increased at each step, which increases u'/S_L^0 and bulk strain rate, and, therefore, enhances the stretch imposed on the flames under study.

Probability density functions of S_T and Z_f for three different fuel mixtures at increasing u'/S_L^0 are shown side-by-side in Figs. 8(a)–8(f). The key features of S_T PDFs are the most probable velocity (expected velocity) ($\langle S_T \rangle$), and the distribution of PDFs compared to S_L . In general, increasing u'/S_L^0 , increases leading edge displacement velocity, as well as local consumption speed in turbulent premixed flames, which is in agreement with previous studies, for example, see Refs. [12,14], and [20].

With increasing u'/S_L^0 , PDFs of S_T are widened and move toward higher velocities. In H_2 -air and CH_4 -air flames with $Le \leq 1$, as u'/S_L^0 increases, PDFs of S_T significantly widen, and $\langle S_T \rangle$ considerably passes S_L values, which indicates the propensity of flames with $Le \leq 1$ to burn faster and to move upstream toward

the unburned mixture. While normalized $\langle S_T \rangle$ is higher in H_2 -air ($Le \ll 1$) compared to CH_4 -air flames ($Le \approx 1$) at constant turbulence, the differences are smaller than the change in turbulent burning rates seen in PDFs of Z_f shown in Figs. 8(d) and 8(f). Furthermore, in C_3H_8 -air flames ($Le > 1$), with increasing u'/S_L^0 , PDFs of S_T only slightly move toward higher velocities. It should be noted that S_T is normalized by S_L that has been corrected for density changes from room temperature to 576 K, which is the temperature at which the oil droplets evaporate.

Probability density functions of Z_f for three different fuel mixtures at increasing u'/S_L^0 are shown in Figs. 8(b), 8(d), and 8(f), where $Z_f = 0$ is located at the exit plane of the bottom nozzle. These PDFs are rich in physical information, and give statistics of the flame's location distribution and range of movement. The most probable flame location (expected flame location) ($\langle Z_f \rangle$) and the flame brush thickness (δ_T) can be extracted from these PDFs. δ_T is defined as: $\delta_T = \pm 2 \times \sigma$, where σ is the standard deviation of the flame location PDF distribution. δ_T contains 95.4% of the observed Z_f values. Furthermore, the skewness of the PDFs indicate a preference for the flame to locate upstream or downstream of $\langle Z_f \rangle$. By increasing bulk flow velocity and u'/S_L^0 , turbulent flames are subjected to a steeper average velocity gradients, which pushes the flames toward the hot stagnation surface, and PDFs are widened.

In order to quantify these statistics, $\langle Z_f \rangle$ correlations at increasing u'/S_L^0 are summarized in Fig. 9. Figure 9(a) illustrates that increasing u'/S_L^0 , and stretching the flame through increasing bulk hydrodynamic strain, as well as turbulence stretch effects, significantly affects the propagation of various fuel mixtures with distinct Le. With increasing u'/S_L^0 , C_3H_8 -air flames ($Le > 1$) are skewed and move significantly downstream due to larger than unity Le. In mixtures with $Le > 1$, thermal diffusion from the positively stretched portion of the turbulent flame front is larger than fuel diffusion into the stretched area. The rate of thermal energy loss is greater than chemical energy gain provided by molecular diffusion into the reaction zone, which reduces the temperature and results in decreasing the flame speed, and consequently, the flame moves downstream. In CH_4 -air flames with $Le \approx 1$, this relocation is less pronounced with steepening average velocity gradients, since the molecular transport into the reaction zone is balanced with thermal diffusion from the reaction zone, and the flame temperature corresponds to T_{ad} .

However, as illustrated in Figs. 8(f) and 9(a), H_2 -air flames remain stationary up to very high bulk velocities ($U/S_L^0 = 42.9$ and $u'/S_L^0 = 16.2$), which shows that mixtures with $Le \ll 1$ are sensitive to stretch effects due to differential diffusion, and the flamelets make larger incursions upstream against the steepening velocity gradient. This is clearly seen in Fig. 8(f), where PDFs of flame location in the case of H_2 -air flames, are spread closer to the bottom nozzle, and Z_f/d_N obtains values as small as 0.25, at increasing u'/S_L^0 . In mixtures with $Le \ll 1$, while the flame front is positively stretched, molecular diffusion into the leading points of the flame is larger than thermal diffusion losses, which increases the local equivalence ratio (ϕ), and consequently, temperature and flame speed increase. It is also indicated in Fig. 9(a) that, at the highest U/S_L^0 and u'/S_L^0 tested in this study, Z_f is close to the stagnation surface in all mixtures due to a very high bulk flow velocity.

Figures 8(f) and 9(a) further validate a significant increase in turbulent burning rates in mixtures with $Le \ll 1$ at increasing bulk flow velocity and u'/S_L^0 , as the flames remain stationary at steepening average velocity gradients. This increase in local turbulent burning rates (and consequently, global turbulent burning rates) is

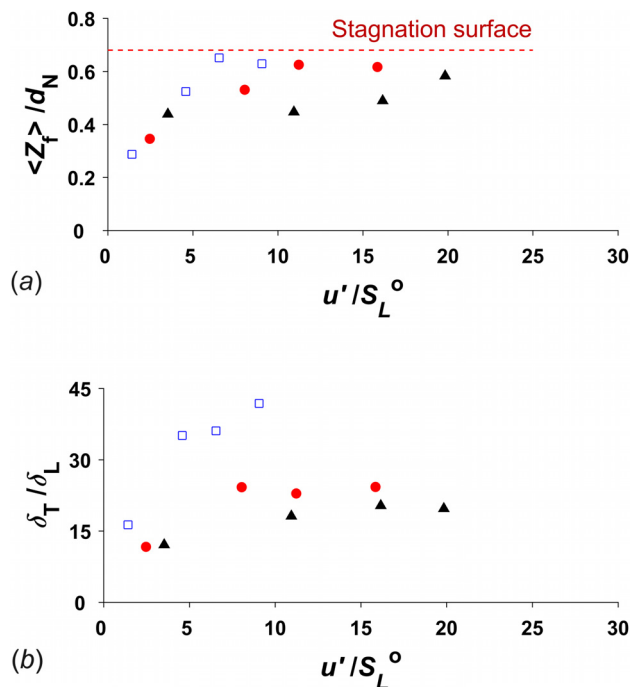


Fig. 9 (a) Most probable flame location ($\langle Z_f \rangle$) and (b) flame brush thickness (δ_T) correlations at increasing u'/S_L^0 : C_3H_8 -air (\square), CH_4 -air (\bullet), and H_2 -air (\blacktriangle) flames

thought to be due to both an increase in local turbulent displacement velocities due to the effects of differential diffusion and stretch sensitivity (as shown in Fig. 8(e)), as well as an increase in flame surface density due to an enhancement in local flamelet curvature, as discussed in Ref. [20].

Flame brush thickness (δ_T) increases with increasing u'/S_L^0 as seen in Fig. 9(b). In mixtures with $Le > 1$, δ_T increases faster with increasing u'/S_L^0 , compared to $Le \approx 1$ and $Le \ll 1$ mixtures, respectively. Thickening trend of δ_T with u'/S_L^0 is in agreement with previous studies, see, for example, Refs. [36] and [43].

3.2 Results and Discussion: Computations. Computations were carried out for the lowest and the highest turbulence intensities for each fuel. Prior to turbulent combustion calculations, counter-flow laminar flames were computed using Cantera in physical space with differential diffusion effects included via detailed chemistry. The Cantera results indicate qualitatively similar behavior to the experiment with respect to flame stabilization at low and high strain rates and follow the trends seen in Fig. 8. At low strain rate, C_3H_8 -air flame stabilizes first, followed by CH_4 -air and H_2 -air flames, though the differences are small. At the highest strain levels, all flames stabilize close to the stagnation plane due to a very high bulk flow velocity.

Figures 10(a) and 10(b) compare the laminar flame profiles of temperature rise (x axis is the distance between the two nozzles) in the left column. At low strain conditions, the highly reactive C_3H_8 -air jet ignites well before the other two fuels. A "bump" in its profile is seen before the post-flame region merges with the hot products from the top nozzle. CH_4 -air flame shows a much smaller bump, and the temperature rise for the lean H_2 -air case cannot be noticed, due to its low T_{ad} . Nevertheless, the computations show a small, but non-negligible reaction rate within the flame-front, as seen in Fig. 11(a), which increases with strain rate (Fig. 11(b)).

In Figs. 10(c) and 10(d), the effect of turbulence intensity on the temperature profiles can be seen. Whereas, there is a certain distance the unburned reactants travel along the axis between the two nozzles ($\approx 0.4 (Z_f/d_N)$), a temperature rise is noticed as soon as the reactants exit the bottom nozzle. This is of chemical origin and not due to mixing, as the turbulent chemical source terms,

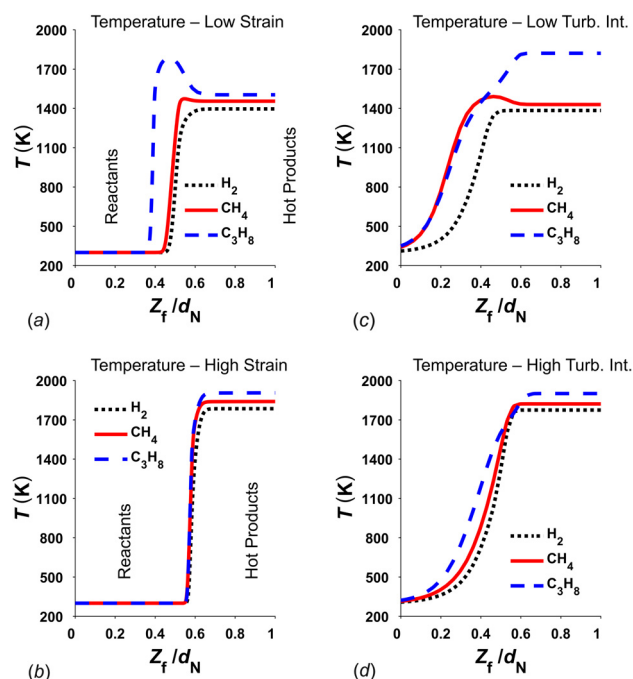


Fig. 10 Effect of strain and turbulence intensity on temperature profiles

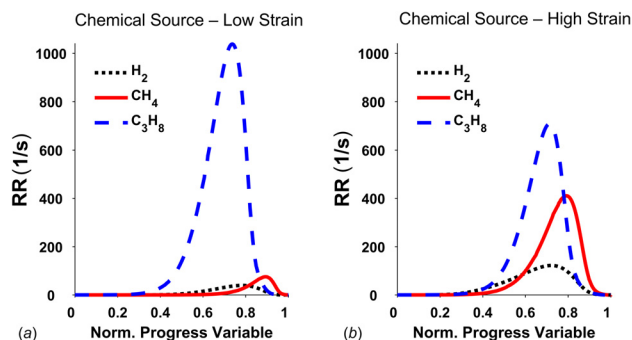


Fig. 11 Effect of strain on laminar chemical source of progress variable

shown in Figs. 12(a) and 12(b), indicate a ramping up as soon as the reactants exit the nozzle. The H_2 -air flames are an exception, however. The temperature rise is markedly slower relative to the others, most likely due to its very lean condition ($T_{ad} \sim 898$ K), and stabilized by a much cooler (1386 K) stream of products. At high strain values, all flames stabilize at the same location indicating that bulk strain effects appear to dominate differential diffusion. For the selected cases, the effect of turbulence intensity coupling with differential diffusion effects is not immediately obvious from the computations for the lowest and the highest turbulence intensities and more cases will need to be computed to isolate the fuel influences.

The flame location and brush thickness may be estimated using the variance predictions. Figures 12(c) and 12(d) show that H_2 -air flames exhibit the largest variance at low, as well as, high turbulence levels. There is relatively less difference between the hydrocarbon flames, and the differences in Fig. 12 may not be explained independently of the laminar hot product boundary conditions. With respect to flame location, flames move downstream as in the experiments, but not to the same extent. At low intensity, the peaks of the reaction rate (a measure of where the flame front is on average) plots in Figs. 12(a) and 12(b), exhibit correct trends compared to the experiment: H_2 -air flames are slightly more downstream compared to CH_4 -air and C_3H_8 -air flames, which

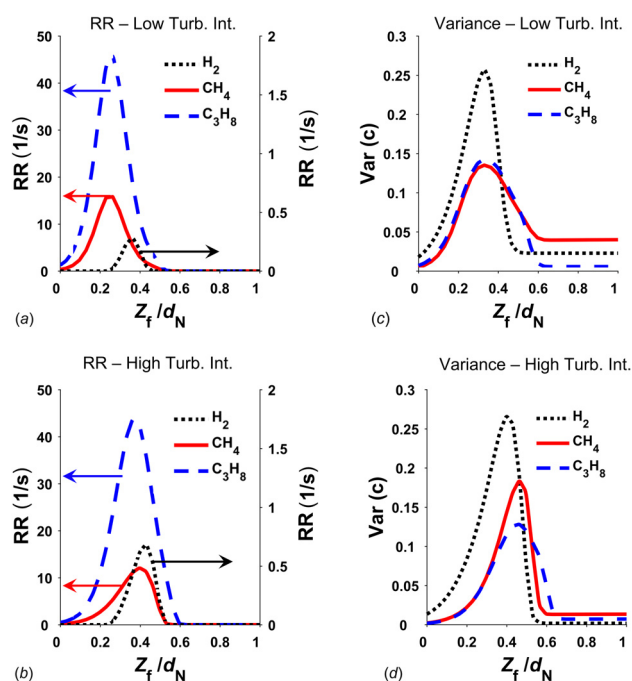


Fig. 12 Turbulent flame location and brush thickness

essentially coincide with respect to their statistically most likely location, as shown by the experimental PDFs of Z_f . At higher turbulence intensity, the flames (especially C_3H_8 -air) do not move as far downstream as the experiments indicate, although their locations relative to each other are in reasonable agreement with the experiment. At present, the reason for this deviation from experiment is unclear, but given the differences between unity and non-unity Le solutions, it is expected that the effects of differential diffusion are significant for this flame configuration. Three-dimensional effects may also be a reason.

The combustion model, as far as the default implementation in FLUENT is concerned, treats the flame as a passive scalar with the influence of fuel isolated to the chemical source term. The dependence of the molecular diffusivity of c and flamelet generation on differential diffusion, as well as scalar dissipation effects in transport of c''^2 must be examined before a comprehensive understanding can emerge. The present calculations also show that the flames are more susceptible to straining effects, as the laminar flame simulations follow the experiment quite well.

4 Conclusions

Sensitivity to stretch and the effects of differential diffusion of various fuels on propagation and stabilization of turbulent lean premixed flames in the thin reaction zone regime were studied in a reactants-to-product counter-flow apparatus. Furthermore, the FGM model was used to simulate three fuels at two turbulence intensities in a RANS context.

The statistics of local instantaneous flame position and turbulent flamelet velocities are observed to be sensitive to the effects of differential diffusion at increasing flame stretch. With increasing flame stretch and due to the effects of differential diffusion in the mixtures with $Le \ll 1$, turbulent flame velocities increase considerably compared to the laminar flame speed, which indicates a propensity of the flamelets to make larger incursions upstream against the steepening average velocity gradient.

Probability density functions of flame location show a significant increase in turbulent burning rates in mixtures with $Le \ll 1$, where H_2 -air flames are almost stationary and compensating for the steepening average velocity gradient imposed by increasing bulk flow, meaning that the turbulent flame speed is increasing to compensate for the increase in the bulk flow velocity. In contrast, the downstream movement of CH_4 -air ($Le \approx 1$) and C_3H_8 -air ($Le > 1$) flames toward the stagnation surface is much steeper compared to H_2 -air flames. However, as illustrated by PDFs of flame velocity, the differences in local turbulent displacement velocities between H_2 -air ($Le \ll 1$) and CH_4 -air ($Le \approx 1$) flames are smaller than the change in turbulent burning rates seen in PDFs of flame location.

The normalized flame brush thickness increases with increasing u'/S_L^0 , and this increase is the largest for C_3H_8 -air flames ($Le > 1$) and the smallest for H_2 -air flames ($Le \ll 1$).

Computations indicate that strained counter-flow laminar flames with detailed chemistry are able to reproduce the experimental trends and turbulence does not mask this behavior. While qualitative trends look encouraging and reproduce the effect of turbulence intensity, fuel influences definitely require the inclusion of differential diffusion for accurate predictions.

Reliable quantitative experimental results, which are quantified and reported as probability density functions using processing techniques proposed in this study, are suitable for validating combustion models that are based on flame-front displacement velocity such as G-equation, reaction progress variable such as FGM-based modeling, and turbulent flame speed correlations.

Acknowledgment

This research was funded by the Natural Sciences and Engineering Research Council of Canada and Siemens Canada Limited under the Collaborative Research and Development program

(NSERC-CRD). The McGill Engineering Doctoral Awards (MEDA) program is also gratefully acknowledged for the support during this research study.

Funding Data

- Natural Sciences and Engineering Research Council of Canada (I242349C0G).
- Siemens Canada Limited (I242215C0G).

Appendix A: Uncertainty in Particle Image Velocimetry

In PIV, it is assumed that the velocity of tracer particles is equal to the flow velocity; however, the velocity-lag of the particles, due to particle-inertia, thermophoretic, and other effects, introduces some uncertainty in the flow velocity measurement. In order to calculate PIV uncertainty in estimating the velocity vector field, the principal sources of uncertainty in particle velocity-lag in these turbulent experiments are considered to be due to Stokes-drag force (F_{SD}) and thermophoresis (F_{TP}) [44]. In this study, thermophoretic force can be neglected due to a low temperature gradient zone ($T < 576$ K). Therefore, considering the Stokes drag force in low Reynolds number flow, the ratio of a tracer particle velocity (u_p) to unburned gas velocity (u_g) is derived, with the details of the various terms available in Refs. [44–46]

$$\frac{u_p}{u_g} = \frac{1}{1 + C_{KW} \tau_s \sigma} \quad (A1)$$

In this equation, C_{KW} is the Knudsen–Weber slip-correction factor [46–48], τ_s is the relaxation time or Stokes time, and σ_u is the fluid velocity gradient. The Stokes time, τ_s , is defined as: $\tau_s = (\rho_p d_p^2) / (18\mu)$, where μ is the unburned gas viscosity, d_p is the oil droplet diameter ($\sim 1 \mu\text{m}$), and ρ_p is the oil density.

Uncertainty details for turbulent combustion experiments are listed in Table 3. As listed in this table, characteristic particle response time is: $\tau_s = 12 \mu\text{s}$, resulting in an uncertainty of less than 1% in a high-turbulence intensity case.

Appendix B: Uncertainty in Flame Surface Tracking

Particle image velocimetry resolution in capturing the flame-front introduces some uncertainty in instantaneous flame-front position measurements using flame surface tracking methods explained in this study. The main sources of this uncertainty are: mean tracer particle distance in the test domain (l_p), oil droplet lifetime at the flame front (droplet evaporation time) (τ_{evap}), uncertainties imposed by filtering processes during post processing procedure (l_{Filt}), and oil droplet illumination in PIV images (l_1).

l_p is calculated through comparisons of saturated and original PIV images, in order to compute seeding density and mean distance between tracer particles. The distance traveled by the flame

Table 3 Uncertainty details of PIV measurements of turbulent premixed flames at increasing U/S_L^0 and u'/S_L^0 for various fuels

	u'/S_L^0	$\tau_s \sigma \times 10^3$	C_{KW}	Uncer. (%)
C_3H_8	1.4	0.74	1.15	0.09
	4.6	2.41	1.15	0.28
	6.5	3.40	1.15	0.39
	9.1	3.98	1.15	0.45
CH_4	2.5	0.64	1.15	0.07
	8.1	2.16	1.15	0.25
	11.2	3.17	1.15	0.36
	15.8	3.55	1.15	0.41
H_2	3.5	0.80	1.16	0.09
	10.9	2.25	1.16	0.26
	16.2	2.86	1.16	0.33
	19.8	3.88	1.16	0.45

Table 4 Various uncertainty sources in flame surface tracking at increasing U/S_L^0 and u'/S_L^0 for various fuels

	u'/S_L^0	l_p/δ_L	l_{evap}/δ_L	l_{Filt}/δ_L	l_1/δ_L	$l_{\text{Total}}/\delta_L$
C_3H_8	1.4	0.887	0.009	0.330	0.264	0.983
	4.6	0.367	0.028	0.330	0.264	0.560
	6.5	0.415	0.045	0.330	0.264	0.594
	9.1	0.245	0.058	0.330	0.264	0.492
CH_4	2.5	0.556	0.006	0.188	0.150	0.606
	8.1	0.261	0.024	0.188	0.150	0.356
	11.2	0.301	0.033	0.188	0.150	0.387
	15.8	0.156	0.042	0.188	0.150	0.290
H_2	3.5	0.487	0.054	0.158	0.126	0.530
	10.9	0.249	0.207	0.158	0.126	0.382
	16.2	0.305	0.316	0.158	0.126	0.483
	19.8	0.187	0.384	0.158	0.126	0.473

front as it sweeps over the oil droplets during τ_{evap} is defined as evaporation distance (l_{evap}). τ_{evap} is calculated as: $\tau_{\text{evap}} = d_p^2/E$, where d_p is the largest oil droplet diameter ($d_p \approx 2 \mu\text{m}$), and E is the evaporation constant [49]. Therefore, $l_{\text{evap}} = \tau_{\text{evap}} \times S_{F_{\text{max}}}$, where $S_{F_{\text{max}}}$ is extracted from PDFs of S_F . Some uncertainties are also imposed through different filters used to enhance the intensity images, main source being the median filter of size 5×5 pixels, which introduces $l_{\text{Filt}} \approx 2.5$ pixels of uncertainty in estimating the flame edge. Furthermore, illumination of typical particles occupy 2 pixels in PIV images ($l_1 \approx 2$ pixels).

The results of uncertainty calculations in flame surface tracking from various sources are listed in Table 4. The total uncertainty is obtained by quadrature: $l_{\text{Total}} = \sqrt{l_p^2 + l_{\text{evap}}^2 + l_{\text{Filt}}^2 + l_1^2}$. As listed in Table 4, $0.290 \leq (l_{\text{Total}}/\delta_L) \leq 0.983$ in these experiments, which shows that the error in flame surface tracking is on the order of, and smaller than, the laminar flame thickness.

References

- [1] Hu, E., Huang, Z., He, J., Jin, C., and Zheng, J., 2009, "Experimental and Numerical Study on Laminar Burning Characteristics of Premixed Methane–Hydrogen–Air Flames," *Int. J. Hydrogen Energy*, **34**(11), pp. 4876–4888.
- [2] Tang, C., Huang, Z., Jin, C., He, J., Wang, J., Wang, X., and Miao, H., 2008, "Laminar Burning Velocities and Combustion Characteristics of Propane–Hydrogen–Air Premixed Flames," *Int. J. Hydrogen Energy*, **33**(23), pp. 4906–4914.
- [3] Boschek, E., Griebel, P., and Jansohn, P., 2007, "Fuel Variability Effects on Turbulent, Lean Premixed Flames at High Pressures," *ASME Paper No. GT2007-27496*.
- [4] Matalon, M., 1983, "On Flame Stretch," *Combust. Sci. Technol.*, **31**(3–4), pp. 169–181.
- [5] Law, C., 1989, "Dynamics of Stretched Flames," *Proc. Combust. Inst.*, **22**(1), pp. 1381–1402.
- [6] Williams, F. A., 2000, "Progress in Knowledge of Flamelet Structure and Extinction," *Prog. Energy Combust. Sci.*, **26**(4–6), pp. 657–682.
- [7] Law, C. K., 2010, *Combustion Physics*, Cambridge University Press, Cambridge, UK.
- [8] Marshall, A., Lundrigan, J., Venkateswaran, P., Seitzman, J., and Lieuwen, T., 2015, "Fuel Effects on Leading Point Curvature Statistics of High Hydrogen Content Fuels," *Proc. Combust. Inst.*, **35**(2), pp. 1417–1424.
- [9] Venkateswaran, P., Marshall, A., Seitzman, J., and Lieuwen, T., 2013, "Pressure and Fuel Effects on Turbulent Consumption Speeds of H_2/CO Blends," *Proc. Combust. Inst.*, **34**(1), pp. 1527–1535.
- [10] Libby, P. A., and Williams, F. A., 1982, "Structure of Laminar Flamelets in Premixed Turbulent Flames," *Combust. Flame*, **44**(1–3), pp. 287–303.
- [11] Chen, Y.-C., and Bilger, R. W., 2004, "Experimental Investigation of Three-Dimensional Flame-Front Structure in Premixed Turbulent Combustion—Part II: Lean Hydrogen/Air Bunsen Flames," *Combust. Flame*, **138**(1–2), pp. 155–174.
- [12] Abdel-Gayed, R., Bradley, D., Hamid, M., and Lawes, M., 1984, "Lewis Number Effects on Turbulent Burning Velocity," *Proc. Combust. Inst.*, **20**(1), pp. 505–512.
- [13] Lipatnikov, A., and Chomiak, J., 2005, "Molecular Transport Effects on Turbulent Flame Propagation and Structure," *Prog. Energy Combust. Sci.*, **31**(1), pp. 1–73.
- [14] Venkateswaran, P., Marshall, A., Shin, D. H., Noble, D., Seitzman, J., and Lieuwen, T., 2011, "Measurements and Analysis of Turbulent Consumption Speeds of H_2/CO Mixtures," *Combust. Flame*, **158**(8), pp. 1602–1614.
- [15] Barlow, R. S., Dunn, M. J., Sweeney, M. S., and Hochgreb, S., 2012, "Effects of Preferential Transport in Turbulent Bluff-Body-Stabilized Lean Premixed CH_4/Air Flames," *Combust. Flame*, **159**(8), pp. 2563–2575.

- [16] Salusbury, S. D., Abbasi-Atibeh, E., and Berghthorson, J. M., 2017, "The Effect of Lewis Number on Instantaneous Flamelet Speed and Position Statistics in Counter-Flow Flames With Increasing Turbulence," *ASME Paper No. GT2017-64821*.
- [17] Yuen, F., and Gülder, O., 2009, "Premixed Turbulent Flame Front Structure Investigation by Rayleigh Scattering in the Thin Reaction Zone Regime," *Proc. Combust. Inst.*, **32**(2), pp. 1747–1754.
- [18] Furukawa, J., Hirano, T., and Williams, F. A., 1998, "Burning Velocities of Flamelets in a Turbulent Premixed Flame," *Combust. Flame*, **113**(4), pp. 487–491.
- [19] Ikeda, Y., Kojima, J., Nakajima, T., Akamatsu, F., and Katsuki, M., 2000, "Measurement of the Local Flamefront Structure of Turbulent Premixed Flames by Local Chemiluminescence," *Proc. Combust. Inst.*, **28**(1), pp. 343–350.
- [20] Driscoll, J. F., 2008, "Turbulent Premixed Combustion: Flamelet Structure and Its Effect on Turbulent Burning Velocities," *Prog. Energy Combust. Sci.*, **34**(1), pp. 91–134.
- [21] Coppola, G., Coriton, B., and Gomez, A., 2009, "Highly Turbulent Counterflow Flames: A Laboratory Scale Benchmark for Practical Systems," *Combust. Flame*, **156**(9), pp. 1834–1843.
- [22] Mastorakos, E., Taylor, A., and Whitelaw, J., 1995, "Extinction of Turbulent Counterflow Flames With Reactants Diluted by Hot Products," *Combust. Flame*, **102**(1–2), pp. 101–114.
- [23] Hampp, F., and Lindstedt, R., 2017, "Quantification of Combustion Regime Transitions in Premixed Turbulent DME Flames," *Combust. Flame*, **182**, pp. 248–268.
- [24] Borghi, R., 1985, "On the Structure and Morphology of Turbulent Premixed Flames," *Recent Advances in the Aerospace Sciences*, Springer, Boston, MA, pp. 117–138.
- [25] Kolla, H., and Swaminathan, N., 2010, "Strained Flamelets for Turbulent Premixed Flames—Part I: Formulation and Planar Flame Results," *Combust. Flame*, **157**(5), pp. 943–954.
- [26] Donini, A., Bastiaans, R., van Oijen, J., and de Goey, L., 2015, "Differential Diffusion Effects Inclusion With Flamelet Generated Manifold for the Modeling of Stratified Premixed Cooled Flames," *Proc. Combust. Inst.*, **35**(1), pp. 831–837.
- [27] van Oijen, J., Donini, A., Bastiaans, R., ten Thije Boonkamp, J., and de Goey, L., 2016, "State-of-the-Art in Premixed Combustion Modeling Using Flamelet Generated Manifolds," *Prog. Energy Combust. Sci.*, **57**, pp. 30–74.
- [28] Coppola, G., and Gomez, A., 2009, "Experimental Investigation on a Turbulence Generation System With High-Blockage Plates," *Exp. Therm. Fluid Sci.*, **33**(7), pp. 1037–1048.
- [29] Goodwin, D. G., Moffat, H. K., and Speth, R. L., 2016, "Cantera: An Object-Oriented Software Toolkit for Chemical Kinetics, Thermodynamics, and Transport Processes. Version 2.2.1," Cantera Developers, accessed Aug. 17, 2018, <http://www.cantera.org>
- [30] Salusbury, S. D., and Berghthorson, J. M., 2015, "Maximum Stretched Flame Speeds of Laminar Premixed Counter-Flow Flames at Variable Lewis Number," *Combust. Flame*, **162**(9), pp. 3324–3332.
- [31] Glawe, G. E., Holanda, R., and Krause, L. N., 1978, "Recovery and Radiation Corrections and Time Constants of Several Sizes of Shielded and Unshielded Thermocouple Probes for Measuring Gas Temperature," NASA Lewis Research Center, Cleveland, OH, Technical Report No. NASA-TP-1099, E-9289.
- [32] Bradley, D., and Matthews, K., 1968, "Measurement of High Gas Temperatures With Fine Wire Thermocouples," *J. Mech. Eng. Sci.*, **10**(4), pp. 299–305.
- [33] Tennekes, H., and Lumley, J., 1972, *A First Course in Turbulence*, MIT Press, Cambridge, MA.
- [34] Hinze, J., 1975, *Turbulence*, McGraw-Hill, New York.
- [35] Balusamy, S., Cessou, A., and Lecordier, B., 2011, "Direct Measurement of Local Instantaneous Laminar Burning Velocity by a New PIV Algorithm," *Exp. Fluids*, **50**(4), pp. 1109–1121.
- [36] Kheirkhah, S., and Gülder, Ö. L., 2015, "Consumption Speed and Burning Velocity in Counter-Gradient and Gradient Diffusion Regimes of Turbulent Premixed Combustion," *Combust. Flame*, **162**(4), pp. 1422–1439.
- [37] Abu-Gharbieh, R., Hamarneh, G., Gustavsson, T., and Kaminski, C., 2003, "Level Set Curve Matching and Particle Image Velocimetry for Resolving Chemistry and Turbulence Interactions in Propagating Flames," *J. Math. Imaging Vision*, **19**(3), pp. 199–218.
- [38] Kolla, H., Rogerson, J., and Swaminathan, N., 2010, "Validation of a Turbulent Flame Speed Model Across Combustion Regimes," *Combust. Sci. Technol.*, **182**(3), pp. 284–308.
- [39] Peters, N., 2000, *Turbulent Combustion*, Cambridge University Press, Cambridge, UK.
- [40] Jella, S., Berghthorson, J., Kwong, W. Y., and Steinberg, A., 2018, "RANS and LES Modeling of a Linear-Array Swirl Burner Using a Flamelet-Progress Variable Approach," *ASME Paper No. GT2018-75896*.
- [41] Nguyen, P.-D., Vervisch, L., Subramanian, V., and Domingo, P., 2010, "Multidimensional Flamelet-Generated Manifolds for Partially Premixed Combustion," *Combust. Flame*, **157**(1), pp. 43–61.
- [42] Goldin, G., Ren, Z., Forkel, H., Lu, L., Tangirala, V., and Karim, H., 2012, "Modeling CO with Flamelet-Generated Manifolds—Part I: Flamelet Configuration," *ASME Paper No. GT2012-69528*.
- [43] Guo, H., Tayebi, B., Galizzi, C., and Escudié, D., 2010, "Burning Rates and Surface Characteristics of Hydrogen-Enriched Turbulent Lean Premixed Methane–Air Flames," *Int. J. Hydrogen Energy*, **35**(20), pp. 11342–11348.
- [44] Berghthorson, J., and Dimotakis, P., 2006, "Particle Velocimetry in High-Gradient/High-Curvature Flows," *Exp. Fluids*, **41**(2), pp. 255–263.
- [45] Egolfopoulos, F. N., and Campbell, C. S., 1999, "Dynamics and Structure of Dusty Reacting Flows: Inert Particles in Strained, Laminar, Premixed Flames," *Combust. Flame*, **117**(1–2), pp. 206–226.
- [46] Allen, M. D., and Raabe, O. G., 1985, "Slip Correction Measurements of Spherical Solid Aerosol Particles in an Improved Millikan Apparatus," *Aerosol Sci. Technol.*, **4**(3), pp. 269–286.
- [47] Talbot, L., 1981, "Thermophoresis—A Review," *Rarefied Gas Dynamics, Parts I and II* (Progress in Astronautics and Aeronautics, Vol. 74), American Institute of Aeronautics and Astronautics, Reston, VA, pp. 467–488.
- [48] Vincenti, W., and Kruger, C., 1965, "Introduction to Physical Gas Dynamics," Wiley, New York.
- [49] Turns, S. R., 1996, *An Introduction to Combustion*, McGraw-Hill, New York.